Evolution of wave spectra in mound-channel wetland systems

Yongqian Yang[a], Jennifer L. Irish[a,*]

[a]*Department of Civil and Environmental Engineering, Virginia Tech, Blacksburg, VA, USA.*

Abstract

Wetlands characterized by vegetation growing in patches, separated by non-vegetated open spaces (channels), widely exist in coastal regions. Since wave energy is an important factor that influences shoreline and wetland stability and causes damage, understanding wave-spectrum evolution in such patchy vegetation is essential to minimizing erosion and coastal hazard. Here, we conducted a numerical investigation on the evolution of irregular waves across various frequency components in mound-channel wetland systems. Simulations with a Boussinesq model showed the impact of patchy vegetation on wave energy was both frequency- and space-dependent. Energy amplification was induced by mound channel wetland systems in specific harmonics and locations. Compared with uniform bathymetry, patchy vegetation on the tops of mounds also influences wave shoaling and nonlinear interaction, intensifying wave energy transfer toward the higher harmonics. This phenomenon became more pronounced for the longer-period incident waves. With increasing incident wave period, mound-channel wetland systems had different impacts on the dominant-frequency and high-harmonic energy; attenuation of the dominant-frequency energy decreased with longer incident periods, while the trend in the high-harmonic energy reversed. This study provides insight regarding wave attenuation by wetlands when there is spatial variability in the wetland configuration. The reduced dominant wave energy by both attenuation and energy transfer may influence sediment transport in mound-channel wetland systems, which is related to long-term stability of shorelines and coastal wetlands.

Keywords: wetlands, wave dissipation, Boussinesq model, wave energy spectra, patchy vegetation

1. Introduction

The present study investigates how mound-channel wetland systems influence wave energy in the nearshore and estuarine areas. There is evidence that coastal wetlands have various ecological benefits for coastal communities, such as providing habitats for flora and fauna, maintaining water quality and enhancing environmental resilience (e.g., Cimon-Morin et al., 2015; Cunniff, 2015; Karjalainen et al., 2016; Silliman et al., 2012). In addition, wetlands can directly mitigate the physical stress of shoreline erosion and wave activity (e.g., Arkema et al., 2013; Costanza et al., 2008; Gacia and Duarte, 2001; Neubauer et al., 2002). According to Cunniff (2015), such a "natural defense" is also more cost-effective than typical hard structures, such as breakwaters and levees.

The subject of wave dissipation by vegetation has attracted numerous studies since the 1980s. Dalrymple et al. (1984) and Kobayashi et al. (1993) derived analytical solutions for the energy decay and wave speed reduction induced by vegetation for monochromatic waves, while Méndez et al. (1999) and Méndez and Losada (2004) extended the models to irregular wave application. In the following years, field studies, laboratory experiments and numerical modeling demonstrated the capacity of vegetation for attenuating wave energy (e.g., Augustin et al., 2009; Loder et al., 2009; Morgan et al., 2009; Wamsley et al., 2010). Recently, the role of vegetation on irregular wave attenuation was found to be frequency-dependent. Bradley and Houser (2009) and Anderson and Smith (2014) observed more energy dissipation in the high-frequency components (compared to low frequencies) by both natural and artificial vegetation. In a field study by Jadhav et al. (2013), the drag coefficient of vegetation depended on wave frequency, and they proposed a frequency-dependent curve for velocity attenuation to better parameterize the drag coefficient across the frequency domain. Wu and Cox (2015) concluded that wave steepness and water depth affected wave energy dissipated by vegetation. Some studies also recognized that wave dissipation was related to vegetation properties like stiffness and density (e.g., Bouma et al., 2005; Paul and Amos, 2011), while Augustin et al. (2009) and Ozeren et al. (2013) observed little

*221E Patton Hall, 750 Drillfield Drive, Department of Civil and Environmental Engineering, Virginia Tech, Blacksburg, VA 24061, USA. Email: jirish@vt.edu.

difference between wave attenuation by rigid and flexible plants. External factors like current and incident wave energy might undermine vegetation's capacity to dissipate waves (e.g., Ondiviela et al., 2014; Paul et al., 2011). However, our understanding of coastal wetlands in mitigating natural hazards is not yet as well-established as it is for hard structures (Cunniff, 2015). For instance, studies on wave dynamics in patchy wetlands are still limited.

In field settings, patchiness is a common property of coastal wetlands (e.g., Rietkerk et al., 2004; Rietkerk and van de Koppel, 2008). The uncertainty of growth and seasonal variability may result in non-vegetated channels in-between vegetation patches. Silliman et al. (2015) and van Wesenbeeck et al. (2008) reported a higher plant growth rate when vegetation was grouped into patches to maximize the positive species interaction. Under appropriate hydrodynamic and abiotic conditions, Bouma et al. (2009) and Balke et al. (2012) observed enhanced sediment accretion induced by the attenuated hydrodynamic energy inside vegetation patches, which induced additional marsh growth. Yet, the dynamics of wave-spectrum evolution in patchy vegetation, which is relevant to the stability of wetlands and wave energy dissipation, is not well understood.

Nonlinear wave interaction is a significant factor in wave-spectrum evolution, especially for shallow-water gravity waves over complex bathymetry. Whalin (1971) observed wave energy transfer toward high frequencies in a series of regular-wave experiments, which was induced by nonlinear wave interaction and uneven bathymetry. Freilich and Guza (1984) derived a one-dimensional Boussinesq model to predict the nonlinear spectral evolution of irregular waves, and observed secondary peaks at higher harmonics of the peak frequency resulting from nonlinear interaction. Liu et al. (1985) extended the work to two horizontal dimensions, which was applicable to more complicated cases. Following studies further demonstrated the relationship between wave-spectrum evolution and nearshore processes, such as wave shoaling, refraction and diffraction (e.g., Eldeberky, 2012; Hamm et al., 1993; Janssen et al., 2008; Norheim et al., 1998). With a mound in the bathymetry, Yeh et al. (1994) observed energy convergence behind a cone-shaped island. In wetlands with complex bathymetry, the presence of patchy vegetation will provide additional attenuation of wave energy. Thus, the evolution of wave spectra becomes more complicated.

This paper is focused on wave evolution in patchy wetlands characterized by vegetated mounds and unvegetated cross-shore channels (mound-channel wetland systems) using numerical simulations with a fully nonlinear and weakly dispersive Boussinesq model. The mound-channel wetland systems are idealized from a prototype engineered wetland in Dalehite Cove, Galveston Bay, TX. In the following, we introduce the applied methodology and present the simulation results. Further insight into the role of mound-channel wetland systems on wave evolution is provided in the discussion, followed by final conclusions.

2. Methodology

2.1. Boussinesq Model

The numerical model used in this study is COULWAVE (e.g. Kim and Lynett, 2011; Lynett et al., 2002), which is based on the depth-integrated Boussinesq-type equations, with sub-models to include the effects of bottom friction, wave breaking and turbulent mixing. This model is fully nonlinear and weakly dispersive, and has been successfully applied in one- and two-dimensional simulations of wave propagation over uneven bathymetry (e.g., Løvholt et al., 2015; Lynett et al., 2010, 2002; Yang et al., 2015). The dimensional governing (continuity and momentum) equations are

$$\frac{\partial \zeta}{\partial t} + \nabla \cdot [(\zeta + h)\mathbf{u}_\alpha] + \mathbf{H.O.T.} = O(\mu^4), \tag{1}$$

$$\frac{\partial \mathbf{u}_\alpha}{\partial t} + \mathbf{u}_\alpha \cdot \nabla \mathbf{u}_\alpha + g\nabla\zeta + R_f - R_b - R_{ev} + \mathbf{H.O.T.} = O(\mu^4), \tag{2}$$

where ζ = free surface elevation, h = local water depth, $\mathbf{u}_\alpha$ = horizontal velocity vector at z_α from still water level and g = gravity. The effects of bottom friction and wave breaking are included in R_f and R_b, and R_{ev} accounts for the vertical and horizontal eddy viscosity of turbulent mixing. $\mathbf{H.O.T}$ represents the higher-order nonlinear and dispersive terms on the order of $O(\mu^2)$, where μ is the ratio of water depth and wavelength ($\frac{h}{\lambda}$). Additional details regarding these terms are described in literature (e.g., Kim and Lynett, 2011; Liu, 1994; Løvholt et al., 2013; Lynett et al., 2002).

To simulate the effect of vegetation in numerical models, various approximations have been applied in previous studies. A straightforward approach is to represent vegetation as increased bottom friction (e.g., Augustin et al., 2009; Blackmar et al., 2013; Loder et al., 2009). This approach works satisfactorily in predicting large-scale flow characteristics, while small-scale patterns adjacent to individual plant stems are not as well resolved. Another approach to approximate vegetation is by including drag force terms, such as in Nepf (2004) and Huang et al. (2011), to explicitly account for the effect of stem density and better capture smaller-scale features. Applying a three-dimensional model, Maza et al. (2015) concluded that simulating the actual geometry of plants provided better prediction of wave forces, compared to the drag force approximation. Recently, Ozeren et al. (2013) and Wu et al. (2016) further demonstrated that vertical variation of vegetation also influenced wave attenuation. In our study, we focus on the wave-spectrum evolution affected by the drag effect of patchy vegetation, where we are interested in the aggregated impact of the vegetation patch on the large-scale flow. Thus, we approximate the vegetation patches as increased bottom friction (R_f in Eq. 2) in the simulations.

2.2. Study Domain

This study expands on the regular-wave experimental findings in Truong et al. (2014) and the numerical simulation findings on wave-induced circulation in Yang et al. (2015). We select the engineered site of Dalehite Cove in Galveston Bay, TX as our prototype, which is composed of constructed vegetated mounds separated by unvegetated channels; vegetation (i.e., higher bottom friction) is specified only at the top of each mound. In nature, similar patchy wetlands also commonly exist (e.g., Rietkerk et al., 2004; Rietkerk and van de Koppel, 2008). The mound spacings (S), water depths (h_o), incident wave heights (H_i) and peak periods of incident waves (T_p) are selected based on the predominant site conditions with Froude scaling (Truong et al., 2014). In the field, the average dimensions of mounds are 35 m for the bottom diameter, 13 m for the top diameter, and 0.5 m in height. The selected geometric scale factor is 1:6.5, while the corresponding time scale factor is 1:2.55. The investigations of Yang et al. (2015) and Truong et al. (2014) were limited to the research of regular waves and three mounds alongshore for all laboratory scenarios. Here, we (a) use TMA wave spectra to simulate more realistic wave conditions (Hughes, 1984), and (b) assume periodic distribution of mounds in the alongshore direction (Fig. 1). To maximize computational resources, the simulations were executed at the same 1:6.5 length scale used in Truong et al. (2014); however, we compared the scaled simulations with real scale simulations to ensure scalability of the results (see Appendix A (Supplementary Materials)). Figure S1 shows the incident wave spectra with peak wave period T_p = 1.5 to 4.0 s, incident wave height H_i = 0.14 m, and offshore depth h_o = 0.50 m. The periodic and infinite distribution of mounds alongshore was simulated by assuming symmetry (depth, free surface and velocity) about the alongshore computational boundaries (i.e., zero normal flux and zero normal gradient at the boundary), which narrowed the domain to save computational time. An absorbing boundary condition was used at the offshore and inshore computational boundaries to eliminate cross-shore wave reflection (e.g., Wei and Kirby, 1995). Consistent with other studies (e.g., Augustin et al., 2009; Blackmar et al., 2013; Yang et al., 2015), the effect of vegetation was included by employing a quadratic bottom friction term in Eq. 2: $R_f = f\frac{u_b|u_b|}{h+\zeta}$, where f is the friction coefficient. Using the laboratory data in Truong et al. (2014), the model setup with COULWAVE employed here was validated and calibrated in Yang et al. (2015) for regular wave conditions in patchy vegetation. Vegetation friction coefficients were calibrated as 0.10 and 0.15 respectively for the 0.50 and 0.36-m depth scenarios. This study applied these calibrated vegetation coefficients to extend the range of the previous research to irregular wave conditions. Hereafter, we refer to the simulations with vegetation represented by higher bottom friction as vegetated scenarios. Table 1 summarizes all simulated scenarios (i.e., mound spacings [$S = 5.48 - 10.02$ m], offshore depths [$h_o = 0.36$ and 0.5 m], incident wave heights [$H_i = 0.07$ and 0.14 m], peak periods [$T_p = 1.5 - 4.0$ s] and vegetation coefficients [$f_{veg} = 0.10$ and 0.15]) in this study. For reference, simulations of horizontal bathymetry without mounds, channels or vegetation were also performed with the corresponding depths and wave conditions. Model validation is presented in Appendix A (Supplemental Materials).

APPROXIMATE LOCATION OF FIGURE 1

Figure 1: (a) Bathymetry (in m) for the 7.02-m mound spacing and 0.50-m offshore depth. Cross-shore channels are along $y = \pm 3.51$ and ± 10.53 m. Vegetation is represented by higher friction on top of the mounds, marked by black dotted circles. Waves propagate from left to right. The mounds are assumed to distribute periodically and infinitely in the alongshore direction. To save computational time, we only model a narrow alongshore-symmetric portion of the domain, and mirror it into infinity in the alongshore direction. (b) Transect of bathymetry along centerline ($y = 0$ m). Horizontal bathymetry without mounds and channels (constant depth after $x = 17.0$ m) is simulated for reference. Grid resolution of 0.05 m was selected to resolve the scale of the mound-channel bathymetry in the simulations.

2.3. Data Analysis

To study the spatial distribution of wave energy, we used 663 model output locations over a sub-domain of 15 m $< x <$ 30 m in the cross-shore direction and from $y = 0$ m to the adjacent cross-shore channel, e.g., $y = 3.5$ m in Fig. 1. Simulation output included time series of free surface elevation and depth-integrated horizontal velocity. Because of symmetry, this sub-domain can be mirrored alongshore to represent the wider domain. Each simulation contained at least 200 individual waves to provide convergence in the estimates of wave spectra. Fast Fourier transform (FFT) was used to obtain wave spectra from the free surface elevation data. The spectra were smoothed by averaging 32 neighboring frequency bands, which resulted in 0.06-Hz frequency resolution. In addition, to quantify wave energy in the harmonic frequencies, we integrated the wave spectra over a few frequency bins centered around the first ($f_1 = \frac{1}{T_p}$), second ($f_2 = \frac{2}{T_p}$) and third ($f_3 = \frac{3}{T_p}$) harmonics to obtain the representative energy, i.e., $\int_{f_i}^{f_u} S_p df$, where S_p is the wave spectrum, f_i and f_u are the lower and upper frequencies around the harmonic. The integration ranges for the first, second and third harmonics were $\frac{0.5}{T_p}$ to $\frac{1.5}{T_p}$, $\frac{1.5}{T_p}$ to $\frac{2.5}{T_p}$ and $\frac{2.5}{T_p}$ to $\frac{3.5}{T_p}$.

3. Results

We applied COULWAVE to simulate all the scenarios in Table 1, then analyzed model output following the methods described above. Figure 2 shows the instantaneous free surface and wave-averaged (over two T_p) current in non-vegetated and vegetated scenario 2 (at time

Table 1: Matrix of simulation scenarios and simulated percent of energy in each harmonic (spatially integrated over area shown in Fig. 8)

Scenario **(m)**	$\boldsymbol{S}$ **(m)**	h_o **(m)**	$\boldsymbol{H_i}$ **(m)**	$\boldsymbol{T_p}$ **(s)**	$\boldsymbol{f_{veg}}$	**Energy in harmonics (%) (NV vs. VG)**					
						1st	2nd	3rd	1st	2nd	3rd
1	5.48	0.50	0.14	2.0	0.10	68	22	5	64	20	4
2	7.02	0.50	0.14	2.0	0.10	69	21	5	68	20	4
3	8.66	0.50	0.14	2.0	0.10	70	21	5	70	21	4
4	10.02	0.50	0.14	2.0	0.10	70	20	4	70	20	4
5	7.02	0.50	0.14	1.5	0.10	78	17	2	77	15	2
6	7.02	0.50	0.14	3.0	0.10	55	24	11	53	24	10
7	7.02	0.50	0.14	4.0	0.10	41	28	15	40	28	16
8	5.48	0.36	0.07	2.0	0.15	56	24	10	54	25	8
9	7.02	0.36	0.07	2.0	0.15	57	25	9	56	25	8
10	8.66	0.36	0.07	2.0	0.15	56	26	9	56	27	9
11	10.02	0.36	0.07	2.0	0.15	58	26	9	58	26	9
12	7.02	0.36	0.07	1.5	0.15	70	20	4	70	19	3
13	7.02	0.36	0.07	3.0	0.15	47	24	13	47	23	13
14	7.02	0.36	0.07	4.0	0.15	38	24	15	38	23	15

S: mound spacing; h_o: offshore depth at wavemaker; H_i: incident wave height; T_p: peak period of incident wave; f_{veg}: increased bottom friction coefficient of vegetation effect; NV: non-vegetated scenario; VG: vegetated scenario.

step $t = 160$ s). Wave shoaling occurs over the mounds with shallower depth, leading to wave height damping by wave breaking on the mound crest ($x = 21$ m). The wave-induced currents converge toward the centerline ($y = 0$ m) in Fig. 2(c,d), and indicate wave refraction behind the mounds ($x = 24$ m). Circulation cells similar to rip current systems are observed farther onshore ($24 < x < 30$ m), with landward currents behind the mounds and seaward currents in the cross-shore channels ($y = \pm 3.51$ m). The alongshore feeder currents from the shadow zone shoreward of the mounds into the channels induce energy amplification in the channels, as shown by the brighter spots (about 50% higher free surface elevation) at $x = 27$ m and $y = \pm 3.51$ m in Fig. 2(a,b). Overall, the wave-induced currents in the vegetated scenario are weaker than in the non-vegetated one. Such current circulation is a significant factor in influencing wave evolution within patchy wetlands. The reader is referred to Yang et al. (2015) for a thorough analysis of the wave setup and wave-induced currents in mound-channel wetland systems.

APPROXIMATE LOCATION OF FIGURE 2

Figure 2: Instantaneous free surface and wave-averaged current for scenario 2 (Table 1) where (a,c) are non-vegetated and (b,d) are vegetated, all at time step $t = 160$ s. Offshore depth $h_o = 0.50$ m, peak wave period $T_p = 2$ s, incident wave height $H_i = 0.14$ m and mound spacing $S = 7.02$ m. Waves propagate from left to right. Black dotted lines depict the ramp and mounds in Fig. 1.

3.1. Significant Wave Height

3.1.1. Impact of mound spacing and depth

Bathymetry characterized by shoals, or mounds, is known to induce wave shoaling, breaking and refraction, consequently inducing current circulation and wave pattern non-uniformity. In this study, the scenarios with different mound spacings and depths provide an insight regarding the extent of the spatial variability of wave height.

Figure 3(a,d,g) show the planform wave height distribution with various mound spacings (i.e., 5.48 m, 7.02 m and 8.66 m) without vegetation. The offshore depth is 0.50 m, with a 2-s peak wave period. Mound-channel bathymetry has a significant influence on wave refraction, shoaling and breaking, leading to alongshore variability in the significant wave height contours. The decreased depths over the mounds cause stronger wave breaking, reducing wave height behind the mounds. In contrast, areas of increased wave height exist in the cross-shore channels (alongshore boundaries of the sub-domain), which is attributed to wave interaction with the nearshore currents induced by the mound-channel configuration (Fig. 2(c)). With increasing mound spacing, both the regions of wave height reduction behind the mounds and the regions of wave height amplification in the channels are pushed farther onshore. According to Yang et al. (2015), mound-channel wetlands generated circulation similar to

APPROXIMATE LOCATION OF FIGURE 3

Figure 3: Contours of local significant wave height normalized by incident significant wave height (unitless) for non-vegetated scenarios (a,d,g) and vegetated scenarios (b,e,h), and percent difference between non-vegetated and vegetated scenarios (c,f,i). Red and blue colors in (c,f,i) indicate wave height increase and decrease by vegetation. Panels (a,b,c), (d,e,f) and (g,h,i) are for mound spacing of 5.48 m, 7.02 m and 8.66 m, respectively, where offshore depth $h_o = 0.50$ m and peak wave period $T_p = 2$ s. Panels (j-r) are the same contours with $h_o = 0.36$ m and $T_p = 2$ s. Waves propagate from left to right. Black dotted lines depict the ramp and mounds in Fig. 1.

rip-current systems, and larger mound spacing left a wider space for circulation development shoreward. As a result, the alongshore feeder flows from the mounds' shadow zones into the channels move shoreward, resulting in wave height amplification farther onshore in the channels.

When water depth decreases, the effect of bathymetry on wave propagation becomes more significant. Figure 3(j,m,p) show the wave height distribution for a 0.36-m offshore depth and the same mound spacings. Compared with the 0.5-m depth scenarios (Figure 3(a,d,g)), the mounds dissipate relatively more wave energy, resulting in relatively lower wave heights at $x > 21$ m. Strong wave height reductions occur behind the mounds. However, unlike the 0.50-m depth, in which the regions of lower wave height widen onshore, these regions in the 0.36-m depth maintain almost a constant width in the cross-shore direction. Moreover, the area of dissipated wave energy behind the mound is less sensitive to the mound spacing. Compared with the deeper scenario, the area of wave height amplification in the channel moves seaward ($x < 23$ m), and increases when the channel is wider.

3.1.2. Impact of vegetation

Figure 3(b,e,h) show the significant wave height distribution for the vegetated scenarios (0.50-m offshore depth), while Fig. 3(c,f,i) show the corresponding percent-difference with respect to the non-vegetated scenarios. While energy dissipation by breaking on the mounds occurs in both the presence and absence of vegetation, when vegetation is introduced the total wave energy dissipation on the mound increases. Thus, vegetation reduces wave height on top of the mounds, and the region of wave damping diverges and extends into the outer shadow zones (hereafter, termed "OSZ"; the blue regions angled to centerline behind the mounds ($x > 23$ m) in Fig. 3(c,f,i)). For small mound spacing, this dissipation expands into the shoreward sides of the channels, but amplifies wave height in the channels next to the mounds (Fig. 3(c)). With wider mound spacings, the amplified wave height in the channels is shifted shoreward in the vegetated scenario. In addition, compared with the non-vegetated scenario, the higher resistance of vegetation reduces the shoreward current behind the mounds by 30% or more, while the alongshore feeder flows are less affected (Fig. 2(c,d)). This results in stronger energy convergence towards $y = 0$ m, resulting in increased wave height of 10 to 40% in some areas shoreward of the mounds in the deeper depth scenarios (Fig. 3(c,f,i)).

With a shallower depth of 0.36 m, the relative impact of vegetation becomes more significant as shown in Fig. 3(k,n,q,l,o,r). Vegetation divides the region of low wave height behind the mound into two parts angled to centerline, $y = 0$ m (Fig. 3(k,n,q)). In the percent-difference contours, wave height reduction in OSZ is more significant than in the 0.50-m depth scenario. When mound spacing increases, wave height amplification in the channels, resulting from the altered circulation patterns induced by vegetation , widens and expands shoreward. On the other hand, the higher vegetation roughness in the shallower depth causes 75% higher dissipation of cross-shore velocity over the mounds (Yang et al., 2015), enabling more energy accumulation shoreward of the mounds. Therefore, wave height amplification by vegetation behind the mounds is also more intense than in the 0.50-m depth scenario; regardless of vegetation scenario there is at least a 30% increase in wave height as shown by the darker hot areas shoreward of mounds in Fig. 3(l,o,r) compared with Fig. 3(c,f,i).

3.1.3. Impact of incident wave period

The simulation results also show the incident wave period (T_p) influences significant wave height distribution. Figure 4 shows selected results, but all results exhibit the same trends with respect to T_p. The shortest incident wave generates more structure than the longer-period waves, such as the slight wave height amplification in OSZ (Fig. 4(a,b)). Regions of low wave height behind the mounds widen with increasing wave period; for the vegetated scenario, this low wave height region diverges into two separated parts when $T_p = 4$ s (Fig. 4(k)). This is similar to the shallower scenario in Fig. 3(n), since the longer wave period approaches the shallow water limit. With longer waves, the effect of vegetation tends to more clearly organize wave height amplification into three regions, i.e., shoreward of the mounds, wave height amplification on the seaward edges of the channels, and wave height damping in OSZ extending into the channels onshore (Fig. 4(k)).

APPROXIMATE LOCATION OF FIGURE 4

Figure 4: Contours of local significant wave height normalized by incident significant wave height (unitless) for non-vegetated scenarios (a,d,g,h) and vegetated scenarios (b,e,h,j) and percent difference between non-vegetated and vegetated scenarios (c,f,i,k). Red and blue colors in (c,f,i,k) indicate wave height increase and decrease by vegetation. Panels from top to bottom are for peak wave periods of 1.5 s, 2 s, 3 s and 4 s, respectively, where offshore depth $h_o = 0.50$ m and mound spacing $S = 7.02$ m. Waves propagate from left to right. Black dotted lines depict the ramp and mounds in Fig. 1.

3.2. Evolution of Wave Spectra

3.2.1. Transfer of wave energy to higher harmonics

The contours of significant wave height only represent the integrated wave energy at each output location in the sub-domain. To investigate the wave energy evolution, wave spectra were extracted from several locations along a cross-shore transect over the mound (i.e., $y = 0$ m); see Figure 5. In all locations, wave energy is transferred from the dominant frequency into the second and third harmonics, which is induced by nonlinear interaction over complicated bathymetry. Wave breaking over the mound significantly reduces the dominant-frequency energy by 51%, while vegetation on the mound's top provides additional attenuation at the higher harmonics (13%). Shoreward of the vegetated mound's bottom ($x = 23.4$ m, Fig. 5(b)), the dominant-frequency energy becomes 20% higher than the shoreward edge of the mound's top ($x = 21.6$ m), which indicates stronger refraction and

APPROXIMATE LOCATION OF FIGURE 5

Figure 5: Wave spectra along the transect over mound (i.e., $y = 0$ m). (a) Non-vegetated scenario; (b) vegetated scenario. Spectra are extracted from locations in front of mound ($x = 17.7$ m), on the mound ($x = 20.4$ m), behind the mound's top ($x = 21.6$ m), and behind the mound ($x = 23.4$ m). Offshore depth $h_o = 0.50$ m, mound spacing $S = 7.02$ m, and peak wave period $T_p = 2$ s.

diffraction, leading to energy convergence, induced by the patchy vegetation (see also Fig. 8(c)).

In order to study the energy evolution of various harmonics over the mound-channel wetland systems, we computed the wave spectra of all 663 output locations and integrated each spectrum over the bins around the first, second and third harmonics (see Section 2.3). Figure 6(a-i) show the wave energy contours of the three harmonics of non-vegetated and vegetated scenarios and the corresponding percent difference, for the 0.50-m depth scenario, while Fig. 6(j-r) show the same results of the 0.36-m depth scenario; Table 1 presents percent of total energy in each harmonic over the area shown in Fig. 8. While most of the energy remains in the dominant frequency (i.e., first harmonic), considerable portions are transferred into the second ($20 - 25\%$) and third ($5 - 10\%$) harmonics. Such energy transfer across frequencies is attributed to various factors, including the bathymetry itself, the presence of vegetation, induced currents and wave steepening, and nonlinear interactions. At the higher harmonics, with respect to the non-vegetation scenarios, vegetation reduces the energy over a larger area (Fig. 6(f,i,o,r)). This implies that vegetation reduces wave energy at higher frequencies, which is consistent with previous studies (e.g., Anderson and Smith, 2014; Bradley and Houser, 2009; Jadhav et al., 2013; Wu and Cox, 2015). Likely both energy transfer across harmonics (see Section 4.4 below) and direct dissipation of energy in the harmonics, as induced by vegetation, contribute to energy reduction at higher frequencies. However, patchy vegetation does not induce wave energy reduction in all locations or at all harmonics. Rather, with respect to the non-vegetated scenarios, energy amplification by vegetation occurs behind the mounds and in parts of the channels. For the shallower depth (0.36 m offshore), higher vegetation roughness results in larger increases in energy behind

APPROXIMATE LOCATION OF FIGURE 6

Figure 6: Contours of wave energy (in m^2) for non-vegetated scenarios (a,d,g), wave energy (in m^2) for vegetated scenarios (b,e,h) and percent difference between non-vegetated and vegetated scenarios (c,f,i). Red and blue colors in (c,f,i) indicate wave energy increase and decrease by vegetation. Panels (a,b,c), (d,e,f) and (g,h,i) are for wave energy around the dominant frequency, second harmonic and third harmonic, respectively, where offshore depth $h_o = 0.50$ m, peak wave period $T_p = 2$ s and mound spacing $S = 7.02$ m. Panels (j-r) are the same contours with $h_o = 0.36$ m and $T_p = 2$ s. Waves propagate from left to right. Black dotted lines depict the ramp and mounds in Fig. 1. To show spatial variation, color bar ranges differ for different scenario depths and harmonics; see Table 1 for total energy in each harmonic.

the mounds, especially at the higher harmonics (Fig. 6(l,o,r)). These regions extend farther inshore compared to the 0.50-m depth scenario.

3.2.2. Impact of incident wave period

Figure 7 show selected harmonic results for various incident wave periods (i.e., $T_p = 1.5$ s and 4 s) for the 0.50-m depth scenario. With increasing wave period, the nonlinear effects becomes more significant (e.g., Whalin, 1971). In addition, when wave period increases, the incident wavelength approaches the shallow-water limit, causing the relative effect of the mound-channel bathymetry to become more pronounced. As a result, a larger portion of wave energy is transferred into the higher harmonics for the 4-s wave scenario. In the laboratory study of regular wave propagation over bathymetry with parallel circular contours, Whalin (1971) also observed more significant energy transfer across harmonics for longer waves. In addition, with longer incident wave period, there is less similarity between the contours of significant wave height (Fig. 4(j,k)) and energy at the dominant-frequency (Fig. 7(j,k)). Here, most energy in $x < 18$ m and $x > 24$ m is transferred into the second and third harmonics. This implies that energy transfer of a long wave across frequencies is spatially dependent within mound-channel systems. Moreover, for longer waves, the increase of energy shoreward of the mounds and in the channels due to vegetation is mainly in the higher frequencies (Fig. 7(o,r)). In contrast, vegetation reduces energy in the higher harmonics in the shorter-wave scenarios over most of the sub-domain (Fig. 7(f,i)).

APPROXIMATE LOCATION OF FIGURE 7

Figure 7: Contours of wave energy (in m^2) for non-vegetated scenarios (a,d,g), wave energy (in m^2) for vegetated scenarios (b,e,h) and percent difference between non-vegetated and vegetated scenarios (c,f,i). Red and blue colors in (c,f,i) indicate wave energy increase and decrease by vegetation. Panels (a,b,c), (d,e,f) and (g,h,i) are for wave energy around the dominant frequency, second harmonics and third harmonics, respectively, where offshore depth $h_o = 0.50$ m, peak wave period $T_p = 1.5$ s and mound spacing $S = 7.02$ m. Panels (j-r) are the same contours with $T_p = 4$ s. Waves propagate from left to right. Black dotted lines depict the ramp and mounds in Fig. 1. To show spatial variation, color bar ranges differ for different scenario depths and harmonics; see Table 1 for total energy in each harmonic.

4. Discussion

4.1. Non-uniform spatial distribution of wave energy in mound-channel systems

With continuous vegetation in planform, wave propagation through the vegetation field varies less alongshore. As a result, a single cross-shore transect can reasonably represent the wave evolution (e.g., Anderson and Smith, 2014; Koftis et al., 2013; Paul et al., 2011; Tang et al., 2015). For the mound-channel wetland systems in this study, however, the impact of patchy vegetation is spatially dependent. Vegetated mounds directly attenuate the wave-induced current, especially in the cross-shore direction (Fig. 2(c,d) and Yang et al. (2015)), which in turn modifies the patterns of wave breaking and wave refraction. This interaction results in wave energy amplification and damping in different regions, rather than a monotonic decay through a vegetation belt (e.g., Eq. 50 in Dalrymple et al. (1984) and Eq. 17 in Kobayashi et al. (1993)). In other words, the simplified one-dimensional approaches to predict wave propagation over uniform vegetation are not appropriate for assessing wave conditions in patchy wetlands.

4.2. Impact of wetland configuration on wave dissipation

To quantify the effect of mound-channel wetland systems on wave evolution, wave height and wave energy are integrated over the sub-domains of the contours in Section 3, i.e., $\int\int H_s dxdy$ and $\int\int S_h dxdy$, where H_s is the significant wave height and S_h is the energy in the harmonics. Figure 8(a) shows the wave height difference (in %) between mound-channel systems with and without vegetation and horizontal bathymetry (without vegetation, mounds or channels), where negative values indicate reduction caused by the vegetated mounds. It is observed that smaller mound spacing and shallower depth provide higher reduction in wave height overall in the sub-domain. Mound-channel bathymetry is the dominant factor in reducing the overall wave height (9% to 18%), while patchy vegetation provides only a fair contribution ($< 4\%$). The effect of vegetation alone is less sensitive to the mound spacing.

APPROXIMATE LOCATION OF FIGURE 8

Figure 8: (a) Percent difference of significant wave height between mound-channel systems with and without vegetation (hollow symbols), and between vegetated mound-channel systems and non-vegetated horizontal bathymetry (filled symbols). Percent difference of wave energy in the first (solid lines), second (dashed lines) and third (dotted lines) harmonics (b) between mound-channel systems with and without vegetation; (c) between vegetated mound-channel systems and non-vegetated horizontal bathymetry. Legends in panel (b) also apply to panel (c). Circles and triangles are for offshore depth $h_o = 0.50$ m and $h_o = 0.36$ m. Peak wave period $T_p = 2$ s. The percent difference is defined as $\frac{V_{veg}-V_{ref}}{V_{ref}} \times 100\%$, where V_{veg} is the value for vegetated scenarios and V_{ref} is the value for reference non-vegetated scenarios. Negative values indicate reduction by vegetation.

Figure 8(b) shows the percent difference of integrated energy in the harmonics between non-vegetated and vegetated mound-channel systems. The effect of vegetation on overall wave energy within subdomain is frequency-dependent, with more dissipation occurring in the higher harmonics. Similar preferential dissipation of high-frequency spectra was reported in other studies with continuous vegetation (e.g., Anderson and Smith, 2014; Jadhav et al., 2013; Wu and Cox, 2015). In our study, however, patchy vegetation does not dissipate wave energy at all harmonics; a slight energy increase ($< 4\%$) is observed in the second harmonics of the shallower scenario. The maximum reductions by vegetation are 6%, 8%, and 18% for the first, second and third harmonics. The combined effect of vegetation plus the mound-channel bathymetry versus the non-vegetated horizontal bathymetry is shown in Fig. 8(c). Energy reduction by the vegetated mounds is more significant for the shallower depth with narrower mound spacing (up to 30%). In the deeper scenario, rather than being dissipated, more energy is transferred into the higher harmonics by the vegetated mounds, leading to increased energy in the second (2% to 6%) and third (12% to 15%) harmonics. However, energy reduction at the dominant frequency is greater than energy increase at the higher harmonics, so the total wave energy in the subdomain is still attenuated (4%) by the combined effects of patchy vegetation plus mound-channel bathymetry in the deeper scenario (solid circles in Fig. 8(a)).

4.3. Impact of wave period on wave dissipation

Similar spatial integration of wave height and wave energy is performed to show the relationship between incident wave period (T_p) and the wave-spectrum evolution in the subdomain. In Fig. 9(a), the effect of bathymetry and vegetation on wave height is not very sensitive to the incident wave period (variation within 5% from 1.5 s to 4.0 s). Wave height attenuation is not always the largest for the shorter wave-period scenarios; for instance, except for the results shown by the filled circles, wave height damping by mound-channel wetland systems on $T_p = 1.5$ s is less significant than $T_p = 2.0$ s.

APPROXIMATE LOCATION OF FIGURE 9

Figure 9: (a) Percent difference of significant wave height between mound-channel systems with and without vegetation (hollow symbols), and between vegetated mound-channel systems and non-vegetated horizontal bathymetry (filled symbols). Percent difference of wave energy in the first (solid lines), second (dashed lines) and third (dotted lines) harmonics (b) between mound-channel systems with and without vegetation; (c) between vegetated mound-channel systems and non-vegetated horizontal bathymetry. Legends in panel (b) also apply to panel (c). Circles and triangles are for offshore depth $h_o = 0.50$ m and $h_o = 0.36$ m. Mound spacing $S = 7.02$ m. The percent difference is defined as $\frac{V_{veg}-V_{ref}}{V_{ref}} \times 100\%$, where V_{veg} is the value for vegetated scenarios and V_{ref} is the value for reference non-vegetated scenarios. Negative values indicate reduction by vegetation.

Figure 9(b,c) show the relative effects of vegetation and bathymetry on wave energy in the harmonics. In both the non-vegetated and vegetated scenarios, the longer wave scenarios (scenario 7 for the deeper depth and scenarios 13 and 14 for the shallower depth; see Table 1) exhibit more nonlinearity, where more than 50% of the spectral energy is in higher harmonics and, consequently, less energy is at the dominant frequency. Compared with a non-vegetated horizontal bottom (Fig. 9(c)), the vegetated mound-channel system causes higher energy reduction at the dominant frequency, with energy reduction increasing with decreasing period (T_p). For the 0.5-m depth scenarios, energy at the dominant frequency is increasingly transferred to the higher harmonics as T_p decreases for $T_p \geq 3$ s, as much as 5% and 15% respectively into the second and third harmonics. However, the longer 4-s wave scenarios exhibit additional energy loss throughout the spectrum, at the dominant frequency and the higher harmonics. As shown in Fig. 7, energy transfer across the spectrum is less significant for shorter waves. In Fig. 9(c), the amplified high-harmonic energy in the deeper scenario (hollow circles with dashed and dotted lines) implies that modified wave shoaling, wave refraction and current circulation by mound-channel wetlands in turn intensify nonlinear energy transfer across frequencies.

The shallower 0.36-m scenarios (Fig. 9(c)) also supports that vegetated mound-channel systems dissipate energy throughout the wave spectrum for longer incident waves. Here, as with the 0.5-m scenarios dominant energy reduction by the vegetated mound-channel system increases with decreasing T_p in the 0.36-m scenarios. Yet, unlike the deeper scenario, energy is dissipated at the higher harmonics with a general trend of increasing dissipation with increasing T_p.

Compared with the non-vegetated mound-channel scenarios, the vegetation causes a higher energy reduction in the higher harmonics (Fig. 9(b)). When vegetation is included in the mound-channel scenarios, energy dissipation decreases more with decreasing T_p at the higher harmonics ($< 10\%$), while energy dissipation is small and largely insensitive to T_p at the dominant frequency.

4.4. Implications of spectral evolution on sediment transport

For the long-term stability of coastal wetlands, the potential issues of vegetation survival and sediment erosion should be considered. Previous studies illustrated that vegetation grew better in patches (e.g., Silliman et al., 2015; van Wesenbeeck et al., 2008), and the positive feedback of sediment accretion could occur under certain conditions (e.g., Balke et al., 2012; Bouma et al., 2009). According to Diplas et al. (2008), the threshold of sediment motion depended on not only hydrodynamic force magnitude but also duration of peak hydrodynamic force. Previously, Yang et al. (2015) reported the efficiency of patchy vegetation in reducing the overall wave-induced flow velocity, which could lead to weaker hydrodynamic force. In this study, the energy transfer toward higher frequencies in mound-channel wetland systems (Tab. 1) reduces the dominant-frequency wave energy, so the duration of dominant force above the threshold of sediment motion may decrease. On the other hand, the transferred energy to higher harmonics can intensify turbulence at the bed, which may result in stirring and more suspended sediments in water column (e.g., Osborne and Greenwood, 1992). In such a case, sediment might still be washed away by currents, even though the duration above the threshold for sediment motion is reduced. For instance, as discussed in Fig. 8(c) and Fig. 9(c), energy at the higher harmonics is amplified by the vegetated mounds (compared to horizontal bathymetry) in the deeper scenario, which may increase sediment suspension. Therefore, to mitigate sediment erosion of patchy wetlands, besides the reduced hydrodynamic force and duration, reducing the potential for energy transfer to higher harmonics may need to be considered, for example by increasing the height of mounds, which might be equivalent to the the shallower scenario in Fig. 8(c) and Fig. 9(c).

5. Conclusions

Patchy wetlands commonly exist in nature due to natural vegetation growth and seasonal variability, and recent studies have also demonstrated higher growth rate and lower erosion when vegetation is grouped in patches. To improve wetland management and minimize marsh loss in engineering practice, it is necessary to further understand the interaction of waves within these mound-channel wetland systems.

Wave-spectrum evolution in mound-channel wetland systems is spatially dependent, and the patchy vegetation does not decrease wave energy in all frequency components or in all locations. Even with the same incident wave-energy level, wave spectra with different peak periods may result in completely different evolution of wave energy in the frequency domain. The mound-channel bathymetry in this study intensifies nonlinear wave energy transfer toward higher frequencies. Consequently, sediment motion as well as wave impacts onshore are not best characterized by considering significant wave height and dominant period alone. Thus, to improve the efficiency of wetlands in attenuating waves and mitigating coastal hazards (e.g., storm surge), the energy distributions of various incident wave conditions should be considered in engineering practice.

In closing, this study complements our understanding of the evolution of irregular waves in mound-channel wetland systems. Our findings demonstrate that the effect of vegetated mounds on wave energy is frequency- and space-dependent within wetlands, and is not well characterized by monotonic dissipation during propagation. Future engineering practice on wetland management and restoration should account for the interaction between naturally occurring irregular waves, currents and complex wetland configuration to better design for, and predict shoreline and wetland stability. Due to the complexity of wave dynamics in these systems, future work is needed to understand the influence of other factors, such as multiple rows of mounds, extreme wave conditions, and quantification of sediment movement and subsequent erosion of marsh fringe and inshore shorelines. Future studies are also needed to understand the relative scale of mound size (e.g., diameter and height) and incident wavelength, to better inform future engineering practice.

Acknowledgements

This material is based upon work supported by the National Oceanic and Atmospheric Administration, U.S. Department of Commerce, under Award No. NA14OAR4170093 to Virginia Sea Grant; and the National Science Foundation via Grant No. CMMI-1206271. The authors acknowledge Advanced Research Computing at Virginia Tech for providing computational resources and technical support that have contributed to the results reported within this paper. The authors would like to thank Ms. K.A. Duhring for sharing her expertise in shoreline protection with wetlands. Y. Yang would like to thank Dr. P.J. Lynett in University of South California for providing the source code of COULWAVE. Comments from Mr. A. Zainali and Mr. R. Sun on applying the appropriate model parameters are acknowledged.

References

Anderson, M.E., Smith, J., 2014. Wave attenuation by flexible, idealized salt marsh vegetation. Coastal Engineering 83, 82–92.

Arkema, K.K., Guannel, G., Verutes, G., Wood, S.A., Guerry, A., Ruckelshaus, M., Kareiva, P., Lacayo, M., Silver, J.M., 2013. Coastal habitats shield people and property from sea-level rise and storms. Nature Climate Change 3, 913–918.

Augustin, L.N., Irish, J.L., Lynett, P., 2009. Laboratory and numerical studies of wave damping by emergent and near-emergent wetland vegetation. Coastal Engineering 56, 332–340.

Balke, T., Klaassen, P.C., Garbutt, A., van der Wal, D., Herman, P.M., Bouma, T.J., 2012. Conditional outcome of ecosystem engineering: A case study on tussocks of the salt marsh pioneer spartina anglica. Geomorphology 153, 232–238.

Blackmar, P.J., Cox, D.T., Wu, W.C., 2013. Laboratory observations and numerical simulations of wave height attenuation in heterogeneous vegetation. Journal of Waterway, Port, Coastal, and Ocean Engineering 140, 56–65.

Bouma, T., De Vries, M., Low, E., Peralta, G., Tánczos, I., van de Koppel, J., Herman, P.M.J., 2005. Trade-offs related to ecosystem engineering: a case study on stiffness of emerging macrophytes. Ecology 86, 2187–2199.

Bouma, T., Friedrichs, M., Van Wesenbeeck, B., Temmerman, S., Graf, G., Herman, P., 2009. Density-dependent linkage of scaledependent feedbacks: A flume study on the intertidal macrophyte spartina anglica. Oikos 118, 260–268.

Bradley, K., Houser, C., 2009. Relative velocity of seagrass blades: Implications for wave attenuation in lowenergy environments. Journal of Geophysical Research: Earth Surface (20032012) 114.

Cimon-Morin, J., Darveau, M., Poulin, M., 2015. Site complementarity between biodiversity and ecosystem services in conservation planning of sparsely-populated regions. Environmental Conservation , 1–13.

Costanza, R., Pérez-Maqueo, O., Martinez, M.L., Sutton, P., Anderson, S.J., Mulder, K., 2008. The value of coastal wetlands for hurricane protection. AMBIO: A Journal of the Human Environment 37, 241–248.

Cunniff, S.E., 2015. The time to start is now: how implementing natural infrastructure solutions can improve and protect our coasts. Journal of the American Shore & Beach Preservation Association 84, 29–32.

Dalrymple, R.A., Kirby, J.T., Hwang, P.A., 1984. Wave diffraction due to areas of energy dissipation. Journal of waterway, port, coastal, and ocean engineering 110, 67–79.

Diplas, P., Dancey, C.L., Celik, A.O., Valyrakis, M., Greer, K., Akar, T., 2008. The role of impulse on the initiation of particle movement under turbulent flow conditions. Science 322, 717–720.

Eldeberky, Y., 2012. Nonlinear effects in gravity waves propagating in shallow water. Coastal Engineering Journal 54, 1250024.

Freilich, M., Guza, R., 1984. Nonlinear effects on shoaling surface gravity waves. Philosophical Transactions of the Royal Society of London A: Mathematical, Physical and Engineering Sciences 311, 1–41.

Gacia, E., Duarte, C.M., 2001. Sediment retention by a mediterranean posidonia oceanica meadow: the balance between deposition and resuspension. Estuarine, coastal and shelf science 52, 505–514.

Hamm, L., Madsen, P.A., Peregrine, D.H., 1993. Wave transformation in the nearshore zone: a review. Coastal Engineering 21, 5–39.

Huang, Z., Yao, Y., Sim, S.Y., Yao, Y., 2011. Interaction of solitary waves with emergent, rigid vegetation. Ocean Engineering 38, 1080–1088.

Hughes, S.A., 1984. The TMA shallow-water spectrum description and applications. Report. DTIC Document.

Jadhav, R.S., Chen, Q., Smith, J.M., 2013. Spectral distribution of wave energy dissipation by salt marsh vegetation. Coastal Engineering 77, 99–107.

Janssen, T., Herbers, T., Battjes, J., 2008. Evolution of ocean wave statistics in shallow water: Refraction and diffraction over seafloor topography. Journal of Geophysical Research: Oceans 113.

Karjalainen, S.M., Heikkinen, K., Ihme, R., Kløve, B., 2016. Long-term purification efficiency of a wetland constructed to treat runoff from peat extraction. Journal of Environmental Science and Health, Part A 51, 393–402.

Kim, D.H., Lynett, P.J., 2011. Turbulent mixing and passive scalar transport in shallow flows. Physics of Fluids (1994-present) 23, 016603.

Kobayashi, N., Raichle, A., Asano, T., 1993. Wave attenuation by vegetation. Journal of waterway, port, coastal, and ocean engineering 119, 30–48.

Koftis, T., Prinos, P., Stratigaki, V., 2013. Wave damping over artificial posidonia oceanica meadow: A large-scale experimental study. Coastal Engineering 73, 71–83.

Liu, P.L.F., 1994. Model equations for wave propagations from deep to shallow water. Advances in coastal and ocean engineering 1, 125–158.

Liu, P.L.F., Yoon, S.B., Kirby, J.T., 1985. Nonlinear refractiondiffraction of waves in shallow water. Journal of Fluid Mechanics 153, 185–201.

Loder, N., Irish, J., Cialone, M., Wamsley, T., 2009. Sensitivity of hurricane surge to morphological parameters of coastal wetlands. Estuarine, Coastal and Shelf Science 84, 625–636.

Løvholt, F., Glimsdal, S., Lynett, P., Pedersen, G., 2015. Simulating tsunami propagation in fjords with long-wave models. Natural Hazards and Earth System Science 15, 657–669.

Løvholt, F., Lynett, P., Pedersen, G., 2013. Simulating run-up on steep slopes with operational boussinesq models; capabilities, spurious effects and instabilities. Nonlinear Processes in Geophysics 20, 379–395.

Lynett, P.J., Melby, J.A., Kim, D.H., 2010. An application of boussinesq modeling to hurricane wave overtopping and inundation. Ocean Engineering 37, 135–153.

Lynett, P.J., Wu, T.R., Liu, P.L.F., 2002. Modeling wave runup with depth-integrated equations. Coastal Engineering 46, 89–107.

Maza, M., Lara, J.L., Losada, I.J., 2015. Tsunami wave interaction with mangrove forests: A 3-d numerical approach. Coastal Engineering 98, 33–54.

Méndez, F.J., Losada, I.J., 2004. An empirical model to estimate the propagation of random breaking and nonbreaking waves over vegetation fields. Coastal Engineering 51, 103–118.

Méndez, F.J., Losada, I.J., Losada, M.A., 1999. Hydrodynamics induced by wind waves in a vegetation field. Journal of Geophysical Research: Oceans (19782012) 104, 18383–18396.

Morgan, P.A., Burdick, D.M., Short, F.T., 2009. The functions and values of fringing salt marshes in northern new england, usa. Estuaries and Coasts 32, 483–495.

Nepf, H., 2004. Vegetated flow dynamics. Ecogeomorphology of tidal marshes. Coastal Estuar. Monogr. Ser 59, 1735–1745.

Neubauer, S., Anderson, I., Constantine, J.A., Kuehl, S., 2002. Sediment deposition and accretion in a mid-atlantic (usa) tidal freshwater marsh. Estuarine, Coastal and Shelf Science 54, 713–727.

Norheim, C., Herbers, T., Elgar, S., 1998. Nonlinear evolution of surface wave spectra on a beach. Journal of physical oceanography 28, 1534–1551.

Ondiviela, B., Losada, I.J., Lara, J.L., Maza, M., Galván, C., Bouma, T.J., van Belzen, J., 2014. The role of seagrasses in coastal protection in a changing climate. Coastal Engineering 87, 158–168.

Osborne, P.D., Greenwood, B., 1992. Frequency dependent cross-shore suspended sediment transport. 2. a barred shoreface. Marine Geology 106, 22–51.

Ozeren, Y., Wren, D., Wu, W., 2013. Experimental investigation of wave attenuation through model and live vegetation. Journal of Waterway, Port, Coastal, and Ocean Engineering 140, 04014019.

Paul, M., Amos, C.L., 2011. Spatial and seasonal variation in wave attenuation over zostera noltii. Journal of Geophysical Research: Oceans (19782012) 116.

Paul, M., Bouma, T.J., Amos, C.L., 2011. Wave attenuation by submerged vegetation: combining the effect of organism traits and tidal current. Marine Ecology Progress Series 444, 31–41.

Rietkerk, M., Dekker, S.C., de Ruiter, P.C., van de Koppel, J., 2004. Self-organized patchiness and catastrophic shifts in ecosystems. Science 305, 1926–1929.

Rietkerk, M., van de Koppel, J., 2008. Regular pattern formation in real ecosystems. Trends in ecology & evolution 23, 169–175.

Silliman, B.R., van de Koppel, J., McCoy, M.W., Diller, J., Kasozi, G.N., Earl, K., Adams, P.N., Zimmerman, A.R., 2012. Degradation and resilience in louisiana salt marshes after the bp–deepwater horizon oil spill. Proceedings of the National Academy of Sciences 109, 11234–11239.

Silliman, B.R., Schrack, E., He, Q., Cope, R., Santoni, A., van der Heide, T., Jacobi, R., Jacobi, M., van de Koppel, J., 2015. Facilitation shifts paradigms and can amplify coastal restoration efforts. Proceedings of the National Academy of Sciences 112, 14295–14300.

Tang, J., Shen, S., Wang, H., 2015. Numerical model for coastal wave propagation through mild slope zone in the presence of rigid vegetation. Coastal Engineering 97, 53–59.

Truong, M.K., Whilden, K.A., Socolofsky, S.A., Irish, J.L., 2014. Experimental study of wave dynamics in coastal wetlands. Environmental Fluid Mechanics , 1–30.

Wamsley, T.V., Cialone, M.A., Smith, J.M., Atkinson, J.H., Rosati, J.D., 2010. The potential of wetlands in reducing storm surge. Ocean Engineering 37, 59–68.

Wei, G., Kirby, J.T., 1995. Time-dependent numerical code for extended boussinesq equations. Journal of waterway, port, coastal, and ocean engineering 121, 251–261.

van Wesenbeeck, B.K., van de Koppel, J., Herman, P.M., Bouma, T.J., 2008. Does scaledependent feedback explain spatial complexity in saltmarsh ecosystems? Oikos 117, 152–159.

Whalin, R.W., 1971. The limit of applicability of linear wave refraction theory in a convergence zone. Report. DTIC Document.

Wu, W.C., Cox, D.T., 2015. Effects of wave steepness and relative water depth on wave attenuation by emergent vegetation. Estuarine, Coastal and Shelf Science .

Wu, W.C., Ma, G., Cox, D.T., 2016. Modeling wave attenuation induced by the vertical density variations of vegetation. Coastal Engineering 112, 17–27.

Yang, Y., Irish, J.L., Socolofsky, S.A., 2015. Numerical investigation of wave-induced flow in moundchannel wetland systems. Coastal Engineering 102, 1–12.

Yeh, H., Liu, P., Briggs, M., Synolakis, C., 1994. Propagation and amplification of tsunamis at coastal boundaries. Nature 372, 353–355.

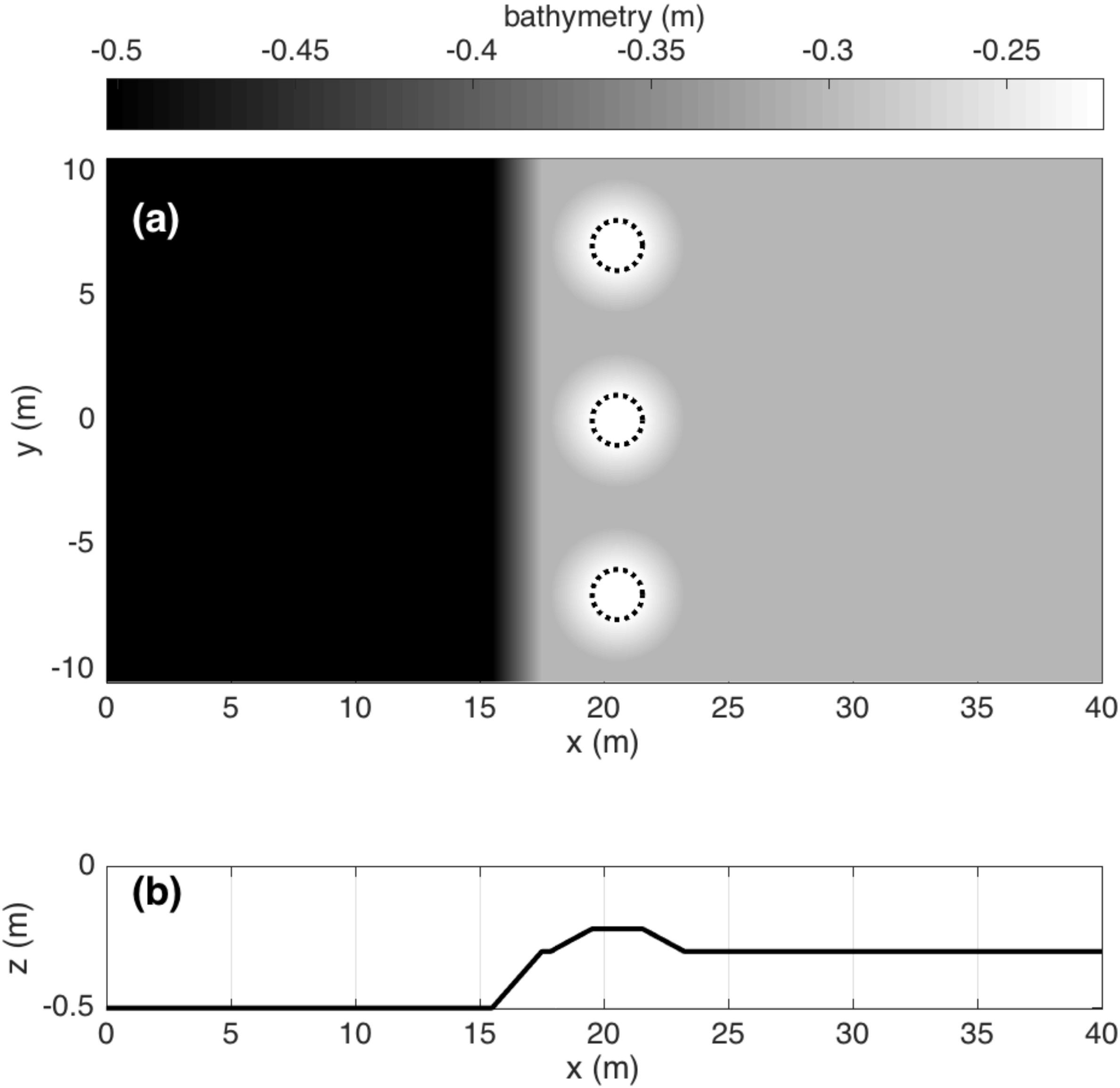
bathymetry (m)
-0.5
-0.45
-0.4
-0.35
-0.3
-0.25
(a)
10
5
0
-5
-10
y (m)
0
5
10
15
20
25
30
35
40
x (m)
(b)
0
-0.5
z (m)
0
5
10
15
20
25
30
35
40
x (m)

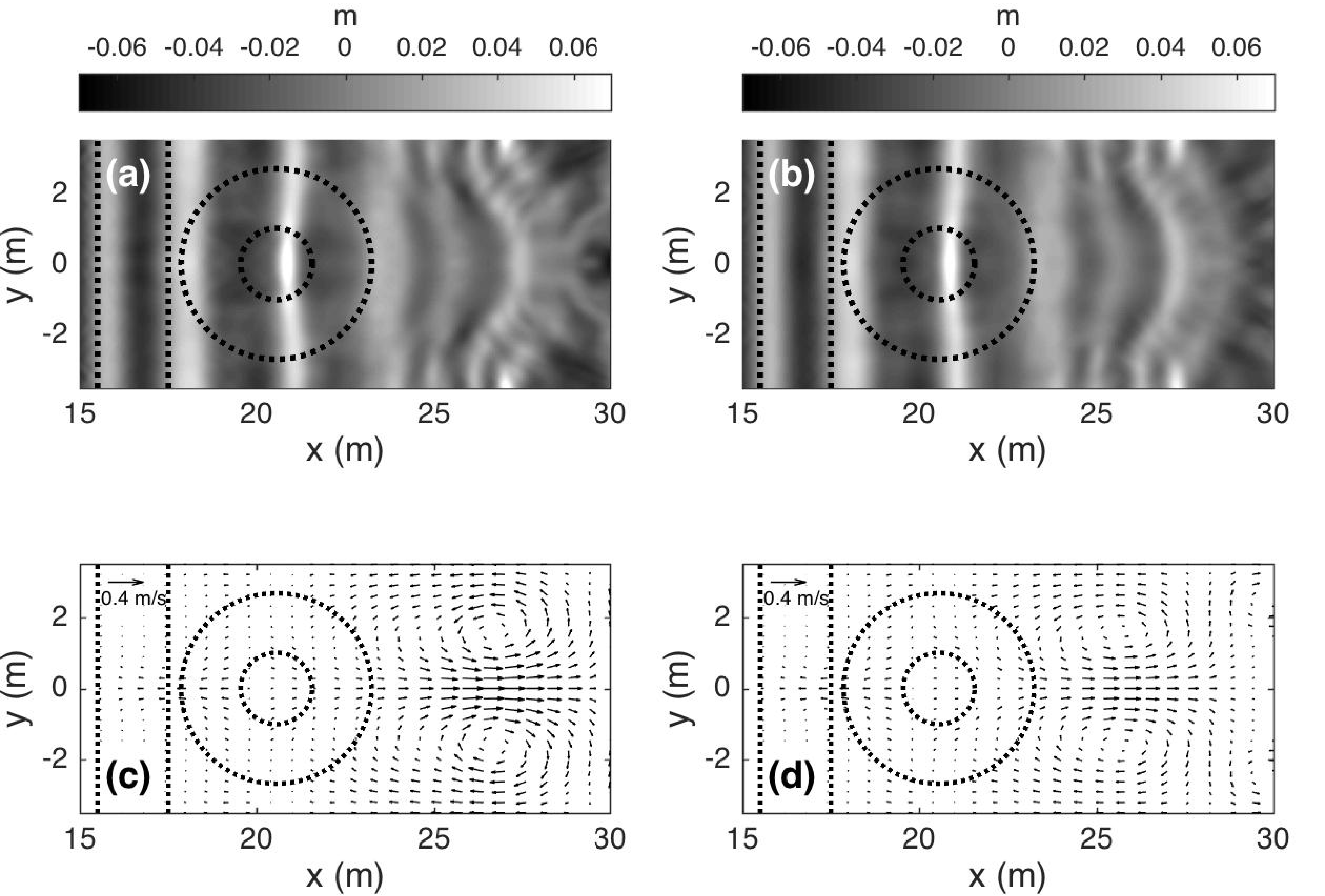
m
-0.06
-0.04
-0.02
0
0.02
0.04
0.06
(a)
(b)
(c)
(d)
0.4 m/s
y (m)
x (m)
15
20
25
30
2
0
-2

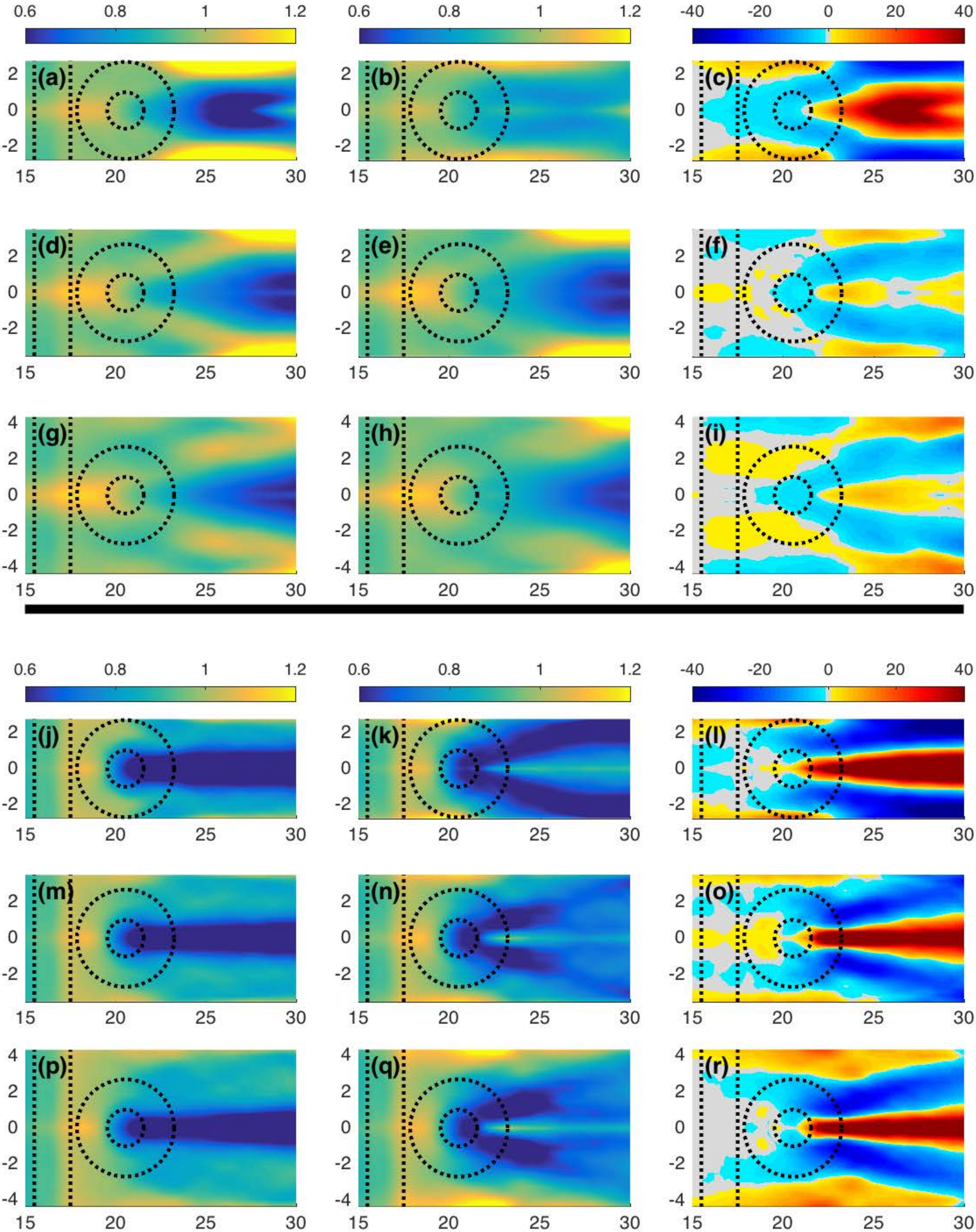

(a)
(b)
(c)
(d)
(e)
(f)
(g)
(h)
(i)
(j)
(k)
(l)
(m)
(n)
(o)
(p)
(q)
(r)

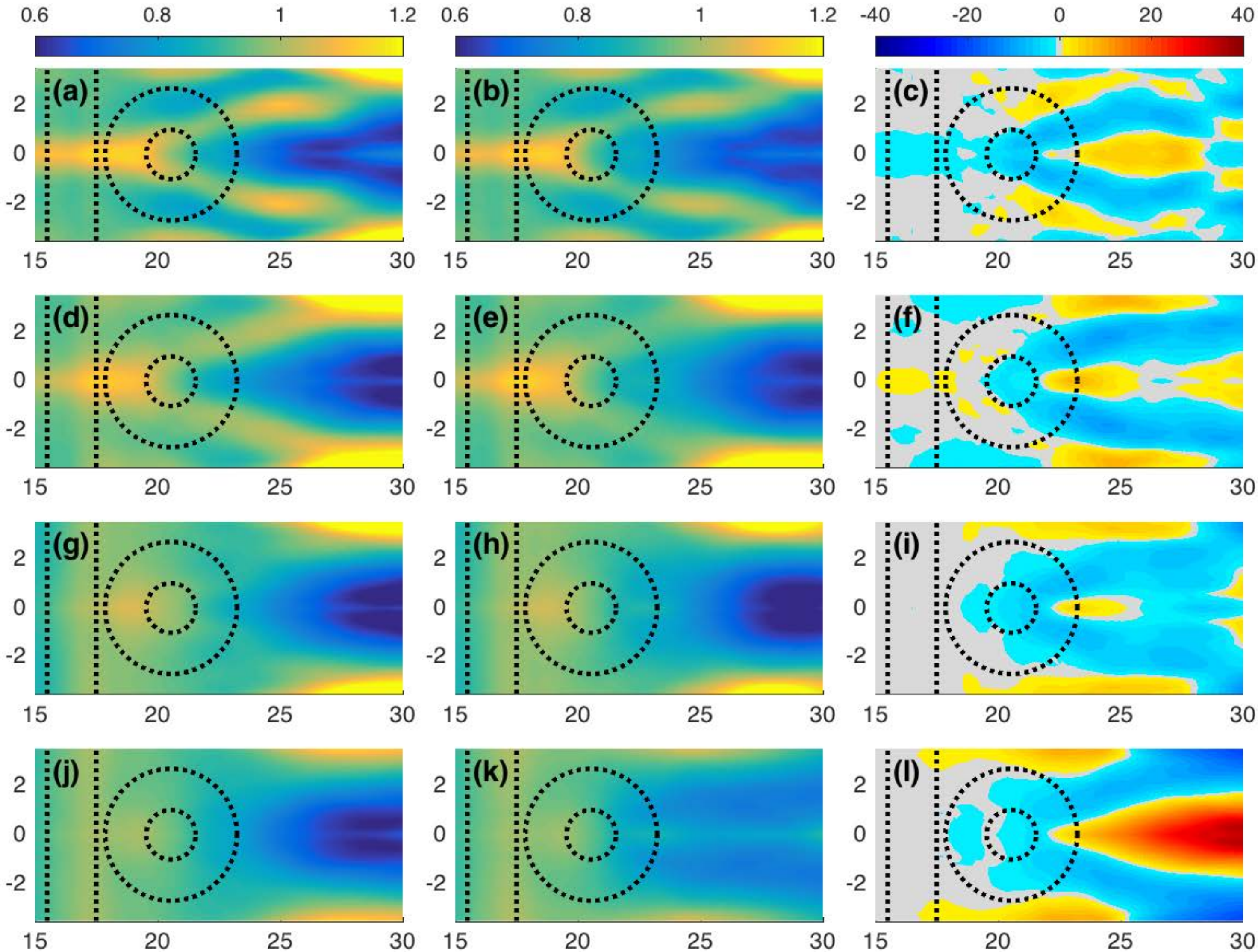

0.6
0.8
1
1.2
-40
-20
0
20
40
(a)
(b)
(c)
(d)
(e)
(f)
(g)
(h)
(i)
(j)
(k)
(l)
2
0
-2
15
20
25
30

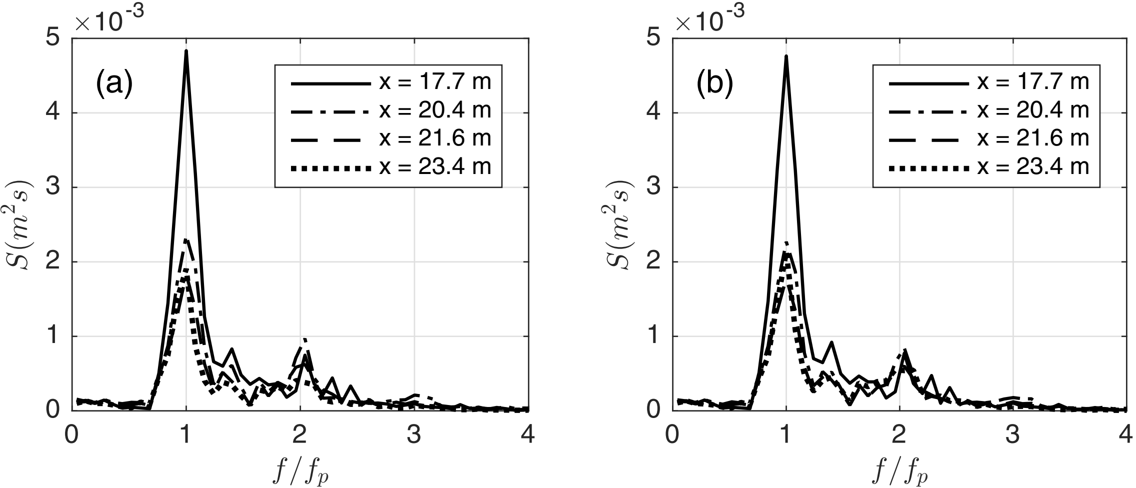

×10-3
5
4
3
2
1
0
(a)
x = 17.7 m
x = 20.4 m
x = 21.6 m
x = 23.4 m
$S(m^2s)$
0
1
2
3
4
f/f_p
×10-3
(b)
x = 17.7 m
x = 20.4 m
x = 21.6 m
x = 23.4 m
$S(m^2s)$
f/f_p

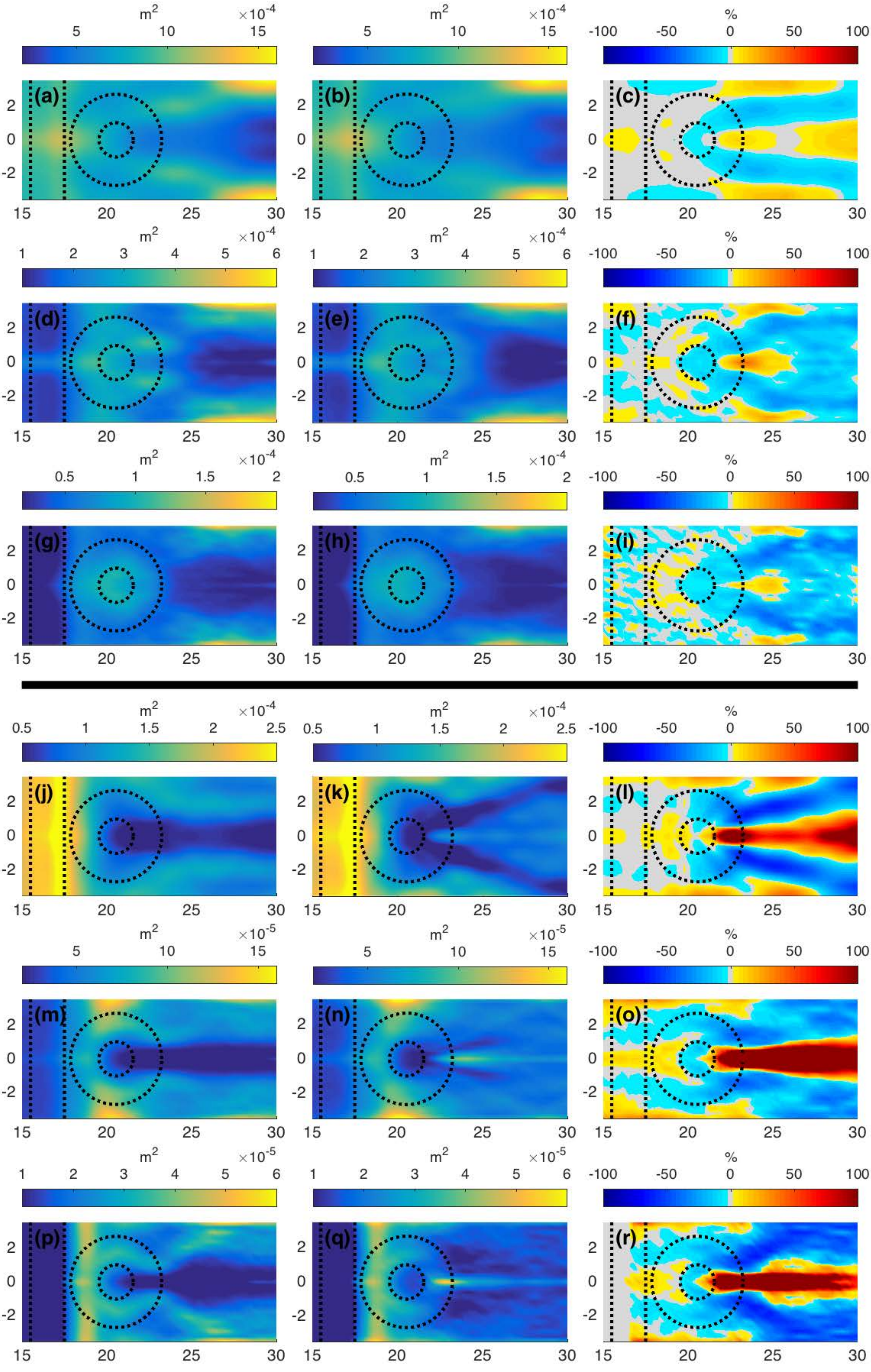

m^2 ×10^{-4}
%
(a)
(b)
(c)
(d)
(e)
(f)
(g)
(h)
(i)
m^2 ×10^{-5}
(j)
(k)
(l)
(m)
(n)
(o)
(p)
(q)
(r)

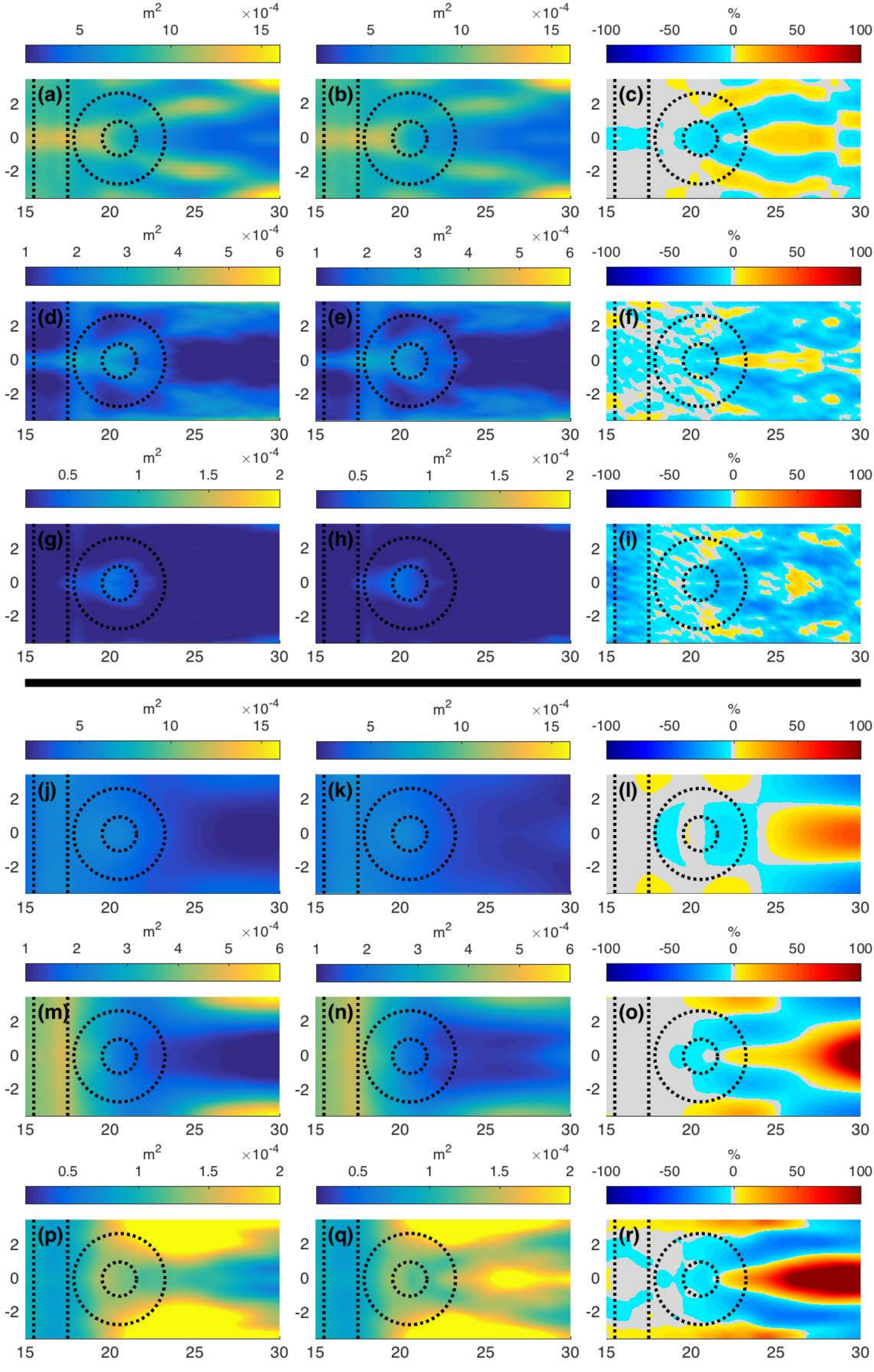

m^2
$\times 10^{-4}$
%
(a)
(b)
(c)
(d)
(e)
(f)
(g)
(h)
(i)
(j)
(k)
(l)
(m)
(n)
(o)
(p)
(q)
(r)

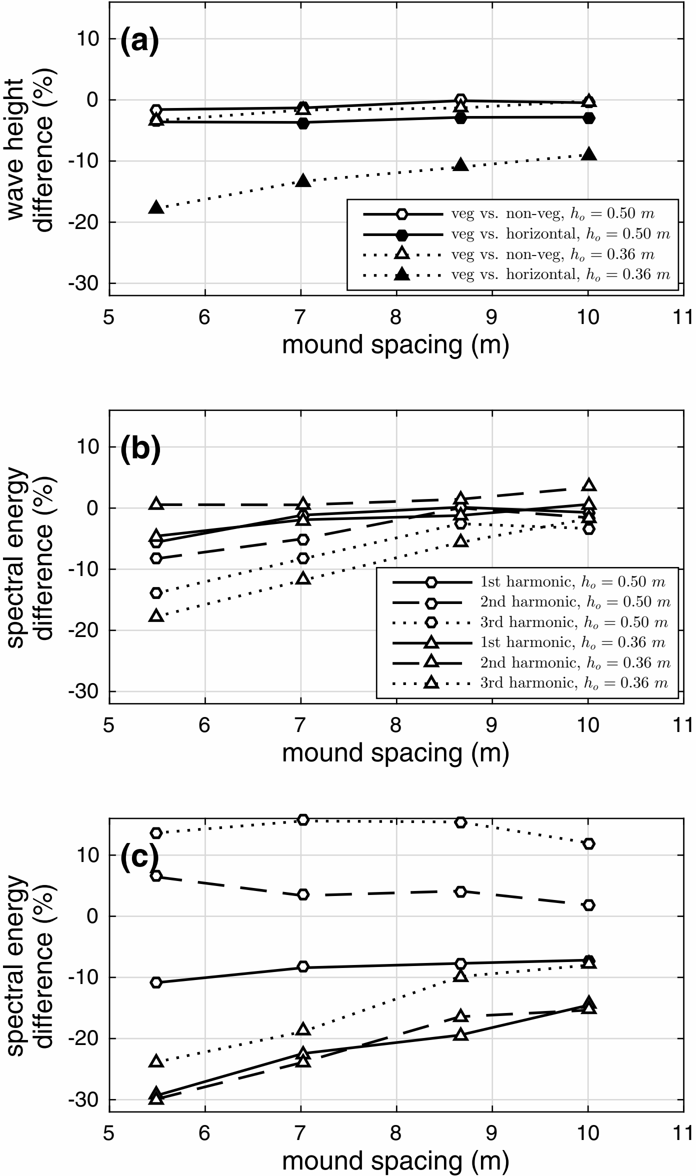

(a)
wave height difference (%)
mound spacing (m)
veg vs. non-veg, $h_o = 0.50\ m$
veg vs. horizontal, $h_o = 0.50\ m$
veg vs. non-veg, $h_o = 0.36\ m$
veg vs. horizontal, $h_o = 0.36\ m$
(b)
spectral energy difference (%)
mound spacing (m)
1st harmonic, $h_o = 0.50\ m$
2nd harmonic, $h_o = 0.50\ m$
3rd harmonic, $h_o = 0.50\ m$
1st harmonic, $h_o = 0.36\ m$
2nd harmonic, $h_o = 0.36\ m$
3rd harmonic, $h_o = 0.36\ m$
(c)
spectral energy difference (%)
mound spacing (m)

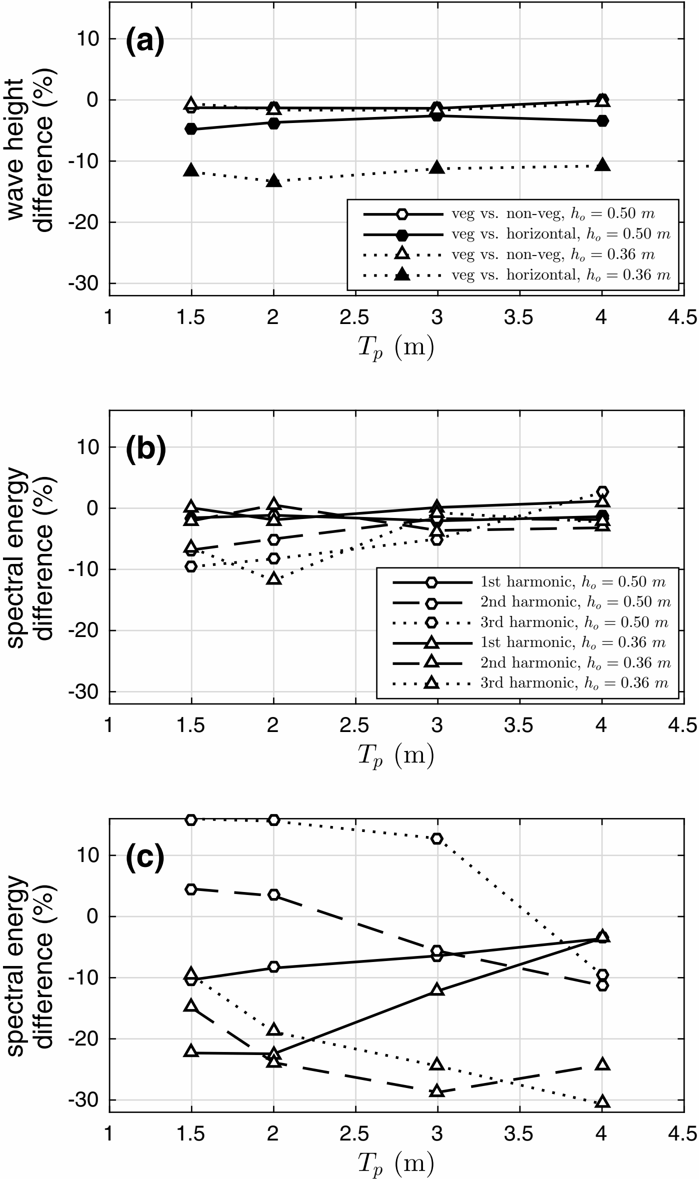

(a)
wave height difference (%)
10
0
-10
-20
-30
1
1.5
2
2.5
3
3.5
4
4.5
T_p (m)
veg vs. non-veg, $h_o = 0.50$ m
veg vs. horizontal, $h_o = 0.50$ m
veg vs. non-veg, $h_o = 0.36$ m
veg vs. horizontal, $h_o = 0.36$ m
(b)
spectral energy difference (%)
1st harmonic, $h_o = 0.50$ m
2nd harmonic, $h_o = 0.50$ m
3rd harmonic, $h_o = 0.50$ m
1st harmonic, $h_o = 0.36$ m
2nd harmonic, $h_o = 0.36$ m
3rd harmonic, $h_o = 0.36$ m
(c)
spectral energy difference (%)